Interacting internal waves explain global patterns of interior ocean mixing: Supplementary Information

Giovanni Dematteis[1,2], Arnaud Le Boyer[3], Friederike Pollmann[4], Kurt L. Polzin[2], Matthew H. Alford[3], Caitlin B. Whalen[5] and Yuri V. Lvov[6]

[1]Università degli Studi di Torino, Torino, Italy.
[2]Woods Hole Oceanographic Institution, Woods Hole, MA, USA.
[3]Scripps Institution of Oceanography, La Jolla, CA, USA.
[4]Institut für Meereskunde, Universität Hamburg, Hamburg, Germany.
[5]Applied Physics Laboratory, University of Washington, Seattle, WA, USA.
[6]Department of Mathematical Sciences, Rensselaer Polytechnic Institute, Troy, NY, USA.

Analysis of nonlinearity level

Coarse-grained and pointwise nonlinearity levels

We define two distinct (coarse-grained) nonlinear times. The first, $\tau_{\rm nl}$, is the timescale of nonlinear evolution of the wave energy spectrum; this is obtained as the ratio between the total energy in a given subregion of spectral space, and the time rate of change of energy in the subregion. The second, $\tau_{\rm res}$, is the energy residence time in the subregion, given by the ratio of the total energy in the subregion, and the total energy flux transferred out of the subregion – i.e., the "sum" of the red arrows going out of the rectangle representing a given subregion in Fig. 2 in Main Text. As was argued by [1], it is the second, the residence time $\tau_{\rm res}$, to be the relevant time for the energy transfers, although the definition of [1] is pointwise in spectral space – see Eq. (1) below. It is sufficient to think of a nonequilibrium stationary state with a nonzero flux to realize that in such case, since the spectrum does not change over time, we have $\tau_{\rm nl} = \infty$, but $\tau_{\rm res}$ will have a finite value that depends on the intensity of the flux. For this reason, we opt to base our analysis of nonlinearity on $\tau_{\rm res}$.

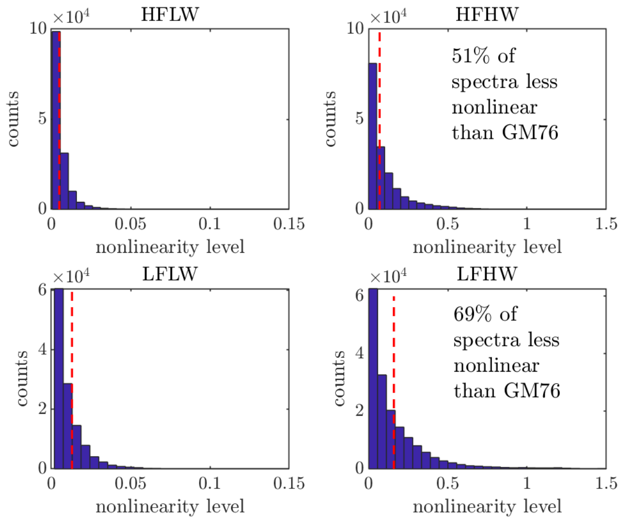

Fig. S1: Histograms of coarse-grained nonlinearity level in the same scale ranges as Fig. 3**D** in Main Text. The HFHW scales have less than 1% of the occurrences at $r_{\rm nl} > 0.5$. The LFHW scales have about 2% of the area at $r_{\rm nl} > 1$ and about 7% of the area is at $r_{\rm nl} > 0.5$. For these coarse-grained metrics, a value smaller than 1 does not ensure weak nonlinearity, since the pointwise metric may be small in a subregion, but well above 1 in another subregion (*cf.* Fig. S2). The coarse-grained nonlinearity level for the GM76 spectrum is indicated by the dashed red lines.

We now compare the estimated residence times with the linear period of internal waves, $\tau_{\rm lin}(\omega) = 2\pi/\omega$, a classical way to assess the nonlinearity strength compared to linear dispersion [2]. In terms of the nondimensional nonlinearity level $r_{\rm nl} = \tau_{\rm lin}/\tau_{\rm res}$, a weakly nonlinear regime is defined by $r_{\rm nl} \ll 1$. In Fig. S1, we show the distributions of $r_{\rm nl}$ in the combined global dataset. At low wavenumber, nonlinearity is always extremely weak. For low wavenumber and high frequency, $r_{\rm nl}$ remains smaller than 0.5, whereas, for high wavenumber and low frequency, the most nonlinear scales, about 2% of the occurrences have $r_{\rm nl} > 1$.

We now turn to a more detailed, pointwise generalization of the residence time, similar to that of [1], illustrated for two reference spectra. The pointwise residence time $\tau_{\rm nl}^{-}(m,\omega)$ is defined as the ratio between the energy density $e(m,\omega)$ and the negative-signed contributions to the rate of change of energy density, $\dot{e}^{-}(m,\omega)$:

$$\tau_{\rm nl}^{-}(m,\omega)=\frac{e(m,\omega)}{|\dot{e}^{-}(m,\omega)|}\,. \tag{1}$$

Again, in order to analyze the weakness of nonlinearity compared to linear dispersion, we compare the residence time with the linear wave period $\tau_{\rm lin}(\omega)$. The pointwise quantities here defined and the nonlinearity parameter $r_{\rm nl}$, defined as

$$r_{\rm nl}(m,\omega)=\tau_{\rm lin}(m,\omega)/\tau_{\rm nl}^{-}(m,\omega)\,, \tag{2}$$

are shown for the two chosen reference spectra in Fig. S2. We observe a sharp discontinuity at $\omega = 2f$. This is due to the disappearance of the PSI transfer mechanism – very efficient for frequencies just larger than $2f$ – at frequencies smaller than $2f$. The most nonlinear scales are located in proximity of $\omega = 2f$, and toward the large wavenumbers.

Clearly, values of the coarse-grained $\tau_{\rm res}$ smaller than unity in a spectral region may still correspond to values larger than unity for the point-wise $\tau_{\rm nl}^{-}$ in some smaller spectral subregion (see Fig. S2). However, the coarse-grained metrics in Fig. S1 are important for a relative comparison among different spectra, noting that we are not able to show a pointwise analysis for the large number of observed spectra. The coarse-grained nonlinearity levels for the GM76 spectrum are shown as dashed red lines in Fig. S1. In the most nonlinear spectral region (low frequency and high wavenumber), about 69% of observed spectra are less nonlinear than GM76, and 31% are more nonlinear than GM76.

Comparison with Holloway (1980)

Here, we discuss the results of [1], where oceanic internal waves were (quite categorically) declared too nonlinear to be described by weakly-nonlinear wave-wave interactions. First, the conclusions of [1], based on results by [3], reached conclusions that reverberate to the present days based on the energy level of the GM76 spectrum alone. Note that the broad distribution of energy levels in the combined global dataset presented in our work is such that more than two thirds of spectra are less nonlinear than GM76 in the most nonlinear range of scales (Fig. S1). Second, our numerical results differ from those of [3]. We show this in detail in Fig. S3. The top panels represent the same quantity $\tau_{nl}(m,\omega) = e(m,\omega)/\dot{e}(m,\omega)$ in [3] (**A**) and in our calculation (**B**). The hydrostatic-balance assumption implemented in our code is well satisfied for the considered range of frequencies up to less than $N/3$, and our result is consistent with recent independent calculations [5–7] (no matter whether near-resonant or exactly resonant, hydrostatic or non-hydrostatic). All of these recent results support our assessment that the time rate of change of energy is negative in a frequency band roughly between $2f$ and $4f$–$5f$. More closely, our result recovers exactly the pattern obtained in [5] in a near-resonant setup. On the contrary, the results of [3] show a negative time rate of change of energy up to frequencies larger than $10f$, where a sharp change of sign departs very markedly from our

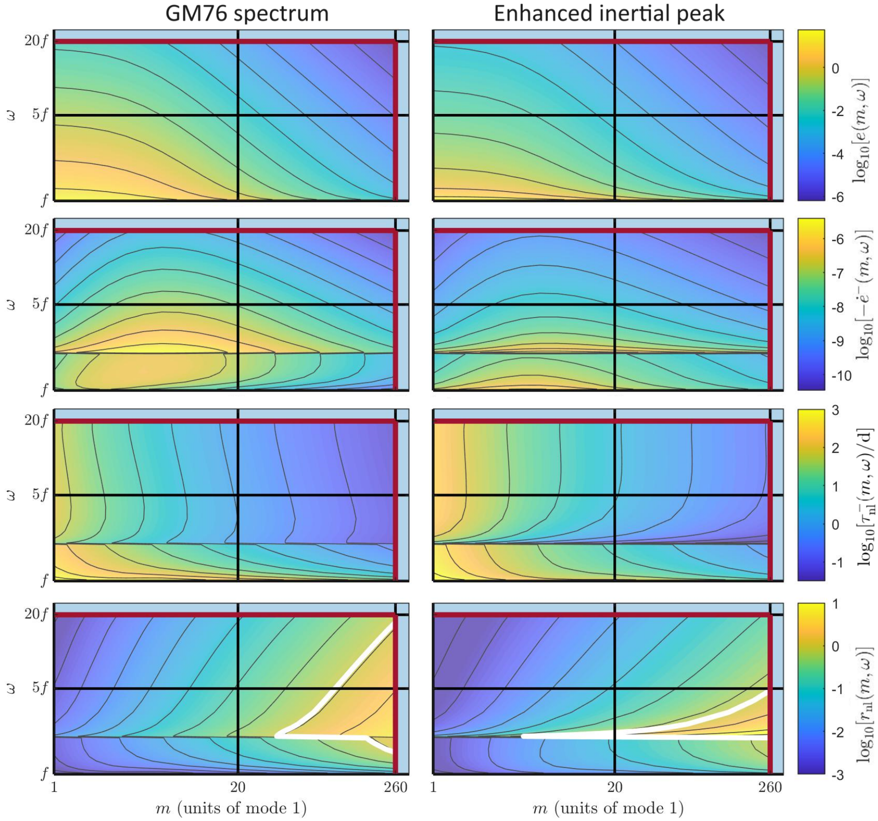

Fig. S2: Left and right panels are for the same two representative spectra shown in Fig. 2 (GM76 and similar spectrum with enhanced near-inertial peak), respectively. From top to bottom, we show color maps of the quantities necessary to evaluate the point-wise nonlinear residence time and nonlinearity level. In the color maps of $\tau_{\rm nl}^{-}(m,\omega)$ we observe time scales that go from hundreds of days for the near-inertial, low-wavenumber waves, up to a few hours for the high wavenumber waves. In the bottom panels, the white contour line is at $r_{\rm nl}(m,\omega) = 1$. To the right of this line, nonlinearity dominates over dispersion, threatening the applicability of weak wave-wave interaction theory. The extra vertical red line in these panels is at $m = m_c/2$ (where m_c is given by Eq. (3) in the main text), the value used in the sensitivity test depicted in Fig. S4 to reduce the amount of strongly nonlinear scales.

results. While we are not able to check the original code of [3], we attribute such change to the abrupt numerical cutoff that apparently was implemented for all frequencies larger $21f$. We suggest that this cutoff is responsible for the abrupt nonphysical upper change of sign – on the other hand, the lower change of sign in proximity of $2f$ is well understood as due to the onset of the PSI branch. We conclude that the results of [3] are not reliable for frequencies

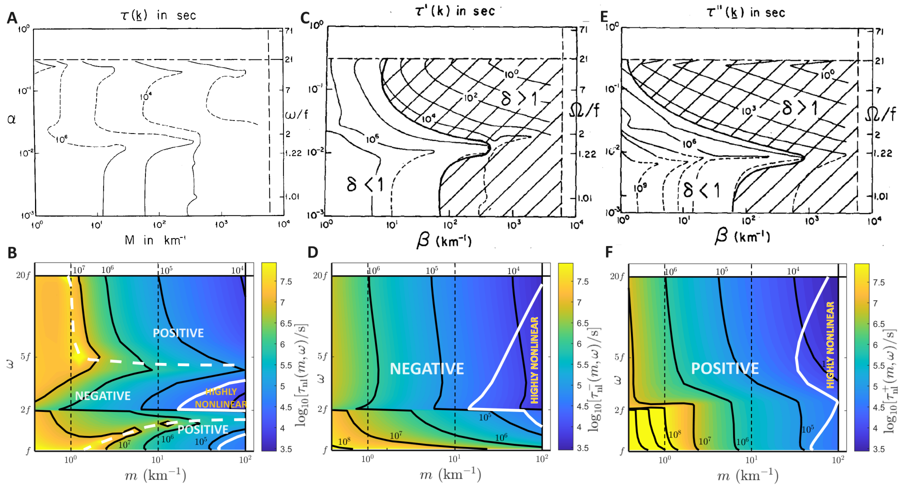

Fig. S3: Detailed comparison between the plots in Holloway (1980) [1], taken from [3] (top), and our results (bottom). The top panels show the spectral evolution timescale τ_{nl}. The negative contributions in **A** (dashed contour lines) extend from below $2f$ up to $15f$, rather than from below $2f$ up to $5f$. The two plots differ for frequency larger than $2f$-$3f$. **C** and **D** should show comparable quantities (residence times), as argued in the text, but they clearly differ in the upper portion of the spectral space. This leads [1] to consider most of the high-frequency region highly nonlinear, whereas we find high nonlinearity at high wavenumber, but not at high frequency. **E** (symmetrization timescale) and **F** (re-filling timescale of an initially depleted mode) do not compare directly, although they show some similarities. Again, though, they lead to drastically different assessments of high-nonlinearity regions. Note that the high-nonlinearity regions in panels **D** and **F** are superposed effects with opposite sign, and the resulting evolution timescale (**B**) is shorter than the nonlinear time in a much smaller region. It is the latter (inverse of the so-called Boltzmann rate) that is usually taken in consideration as a parameter for high nonlinearity in the weak wave turbulence literature [4, 5].

larger than about $3f$ (while they are roughly in agreement with our results for lower frequency).

We did not reproduce the same experiment of decay of a narrow perturbation as in [3] (Fig. S3**C**), but we can associate to this decay timescale the pointwise residence time τ^-_{nl} (Fig. S3**D**), as discussed in the previous section. Again, a clear departure between the two plots is observed at frequencies larger than $2f$. In particular, the "linear time equals nonlinear time" line drawn by [1] on top of the plot by [3] does not have correspondence in our results. The analogue in Fig. S3**D** is the white line on the right side of the plot.

Finally, we report in Fig. S3**E** the experiment by [3] about the symmetrization timescale of an initially asymmetric spectrum, which shows closer qualitative similarity with the timescale $\tau^+_{nl}(m,\omega) = e(m,\omega)/\dot{e}^+(m,\omega)$ in our analysis, where $\dot{e}^+(m,\omega)$ denotes the positive-signed contributions to the rate of change of energy density. τ^+_{nl} is the timescale it takes a wavenumber to restore its initially depleted energy density, re-equilibrating with the rest of the spectrum. Even for this different timescale, the high-nonlinearity levels concentrate on the far right end of the plot, contrary to the line drawn by [1]. In light of our results, and of the quantitative support they find in independent recent analyses [5–7], we consider the quantitative conclusions by [1] unreliable.

For a GM76 spectrum, Fig. S3 shows that when the nonlinear timescales at play become comparable with the linear time, this happens for wavenumbers that are close to the $m_c = 2\pi/10$ m^{-1} boundary. Moreover, cancellations between positive and negative contributions to the time rate of change $\dot{e}(m,\omega)$ are such that the spectral evolution timescale $\tau_{\mathrm{nl}}(m,\omega)$ shown in Fig. S3**B** is shorter than the linear time only in the restricted range of scales in which $\dot{e}(m,\omega) < 0$. In weak wave turbulence it is this timescale $\tau_{\mathrm{nl}}(m,\omega)$ (inverse of the so-called Boltzmann rate [5]) that is usually considered as a proxi for nonlinearity [4]: comparable positive and negative contributions to $\dot{e}(m,\omega)$ (Figs. S3**D** and S3**F**, respectively) will coexist and counter each other decreasing the effective nonlinearity (Fig. S3**B**).

Moreover, the small nonlinear times $\tau_{\mathrm{nl}}(m,\omega)$ in Fig. S3**B** are an indication of the nonstationary conditions represented by the GM76 spectrum. If evolved forward in time, this would lead to a depletion of energy density in the frequencies just larger than $2f$ and at large wavenumber, and to a spectral distribution that is not separable in the frequency-wavenumber space. The observational trace of this specific issue in the form of a “mid-frequency dip” was discussed in section 5.1.2.3 of [5]. In this manuscript, our global-scale approach forces us to necessarily assume separability of spectra in frequency and wavenumber, so that we can approximate 2D spectra by cross-matching independent databases. Considering the time evolution would require high computational cost, and a detailed knowledge of the energy sources of the internal wavefield and of actual 2D spectra – a type of information that is rarely simultaneously available [5]. Such studies, which are the subject of ongoing research, require focusing on few select locations rather than on global patterns, outside the scope of the current work.

The large number of spectra processed in our analysis requires us to assume a large wavenumber scale m_c past which to evaluate the energy transfers. We made the choice of 10 m for this vertical threshold scale, due to its large significance in the literature [5, 6, 8]. We are aware that dealing rigorously with the issue of high nonlinearity would imply a choice of m_c that is case dependent. This would compromise the feasibility of global-scale evaluations such as the ones that we perform.

Here, our justification of this approach has a pragmatic basis. Below, a sensitivity test shows that our evaluations are weakly sensitive to the choice of the m_c threshold. This near-independence of the threshold choice makes our results effectively free of any arbitrary degree of freedom. Therefore, we chose to keep in our analysis spectra that have an elevated energy level and should raise a high-nonlinearity warning. A few considerations are in order: First, in absence of any alternative prognostic fully-nonlinear theories [9], the weakly nonlinear prediction is the only theoretical explanation available that does not include adjustable parameters. Second, when averaging over time and among different regions with similar turbulence production levels, the agreement between our first-principles weakly nonlinear predictions and the phenomenological strain-based FP predictions is striking (see Fig. 3**B** in main text). If anything, this is a clear *a posteriori* indication that weakly nonlinear interactions underly internal-wave driven turbulent mixing in the global ocean interior. Characterizing location-dependent departures due to violation of weak nonlinearity, but also possibly of other assumptions, are outside the scope of this manuscript, and are the subject of ongoing research.

Sensitivity analyses

High-wavenumber boundary

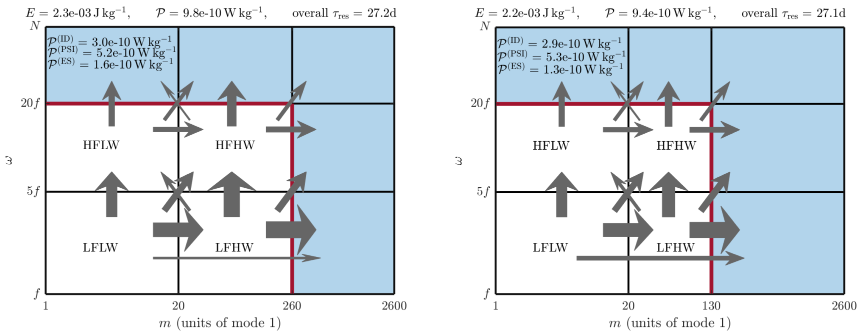

Fig. S4: Sensitivity test of evaluation of TKE production rate upon halving the value of the high-wavenumber boundary with the dissipation region. Both panels are evaluated for the same GM76 spectrum.

In light of our analysis of nonlinearity level, highlighting the presence of high nonlinearity at large vertical wavenumbers, it is important to study the sensitivity of our results with respect to the location of the boundary m_c defining the dissipation region. If the flux across the boundary is insensitive to the position of the boundary itself, we are free to exclude the most nonlinear scales which hinder the weak-nonlinearity assumption. In Fig. S4 we repeat our analysis for the GM76 spectrum, by halving the value of m_c. We show that this changes the calculated value of TKE production rate by less than 5%, adding to the robustness of the theoretical calculation of $\mathcal{P}$. Also, notice that the increased nonlinearity at the transition to strong turbulence in proximity of m_c is expected, since the instability mechanisms at the onset of turbulence itself are strongly nonlinear. It thus appears to be natural to have values of the nonlinearity parameter $r_{\rm nl}(m,\omega)$ of the order of unity in proximity of $m = m_c$.

In order to compute the transfers through the boundary m_c, we have to assign a spectral distribution in the dissipation region, past the m_c boundary. Lacking knowledge, in general, of these scales, operationally we extend the spectral slope past the m_c boundary. A key observation that justifies this operation resides in the fact that the transfers are dominated by local interactions, and we confidently estimate that most of the interactions transferring energy past m_c involve wavenumbers that are smaller than $2m_c$. A sensitivity test performed in [5] shows that cutting off completely all wavenumbers with $m > 2m_c$ implies no perceived change in the time rate of change for wavenumbers with $m < m_c$. We do not repeat such a test here. We opted for this choice for simplicity, since the introduction of a sixth spectral parameter would make a full exploration of the spectral parameter space unattainable by our numerical method. Moreover, the poor observational handle on these small-scale wavenumbers would have made the uncertainty on this extra parameter very high. On the other hand, the physicality of our choice relies on the fairly small bandwith in vertical wavenumber involved in the transfers past m_c, due to the local character of the wave-wave interactions.

Similar in spirit, a sensitivity test on the location of the high-frequency threshold, which we placed at $20f$, was carried out in [10]. They showed that moving the high-frequency boundary past which the energy transfers are computed by a factor of $\sqrt{2}$ implied a total difference in the turbulence production of no more than 10%. We refer to that test without repeating it here, since their non-rotating approximation is retrieved by our high-frequency regime, and our results generalize consistently the results of [10].

We end this section by noting that the weak sensitivity to the location of the spectral boundaries in our framework has to be ascribed to the dominance of local interactions in determining the spectral transfers. This stands in contrast to the eikonal framework, in which large scale separation between small scale waves and large scale background shear implies a high sensitivity to the wavenumber thresholds of scale separation and of wave breaking [11, 12]. The array of sensitivity tests here described ensures the robustness of our quantifications, as they do not depend upon arbitrary degrees of freedom that could serve as tunable parameters. Furthermore, they should not be substantially impacted by the gradual breakdown of weak wave turbulence near the spectral boundary m_c.

Finestructure contamination

The analysis of ocean data is predicated upon a Reynolds decomposition and vertical scale separation, for which we direct the reader to [13] for a discussion of 'best practices'. The most problematic issue here is the assumption that the perturbation fields represent internal wave dynamics. Experience from a variety of internal wave climates away from boundaries demonstrates that this assumption is more of an issue for finescale buoyancy gradients than for finescale shear [14], especially if the data contains healthy near-inertial signatures.

Finescale buoyancy variability may have a quasi-permanent component associated with either (i) the generation of potential vorticity anomalies at boundaries by topographic torques and the consequent injection of those anomalies into the ocean interior [15], (ii) generic upper ocean variability, either resulting from patchiness in forcing and restratification [16] or through the development of submesoscale variability [17], (iii) internal wave-driven scarring of the thermocline on vertical scales larger than those of overturning events [18, section 5.2], and (iv) up-gradient buoyancy fluxes associated with double-diffusive phenomena that spontaneously creates finescale variability [19, 20]. In (i)-(iii) the dynamics of quasi-permanent finestructure is that of either stratified or rotating stratified turbulence, in which a horizontal wavenumber cascade is attained via horizontal stresses and horizontal rate of strain, with vertical coupling at scales limited by shear instabilities [21, 22].

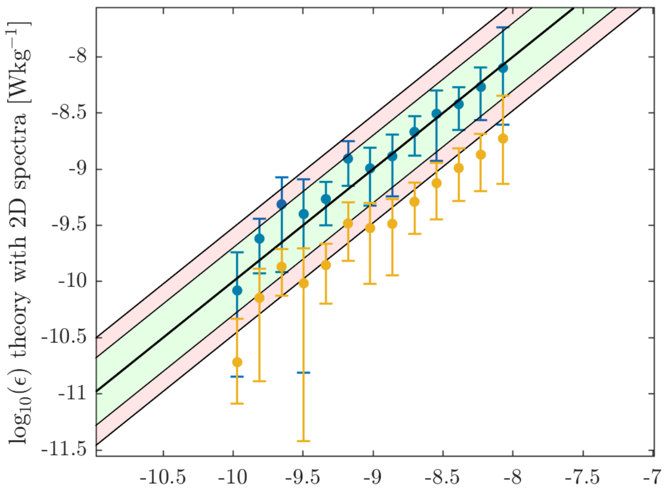

Fig. S5: Sensitivity test upon adding an extra 0.20 to the vertical wavenumber slopes s_m (yellow dots) obtained from the Argo strain spectra, compared to the results in Fig. 3**B** (blue dots), in an attempt to roughly bound the effects of finestructure contamination.

The coupling of internal waves with quasi-permanent finestructure through a wave breaking process (issue (iii)), however, implies our vertical wavenumber power law estimates are likely to be consistently biased high in association with an increasing contribution of quasi-permanent finestructure with increasing wavenumber. There is one reference analysis to constrain this potential bias: this comes from analysis of High Resolution Profiler data in the North Atlantic tracer Release Experiment (NATRE). In this instance, the observed vertical wavenumber spectral slope for velocity is -2.55. After subtracting the quasi-permanent signatures, the exponent is -2.75.

We use this difference as a metric of potential bias, with the insight that the spectral slopes for the NATRE data set are an outlier in vertical wavenumber - horizontal wavenumber space [5] and that such bias cannot be properly assessed without a data set that combines high quality velocity and density finestructure. The result of the analysis upon adding the potential bias of 0.20 to the vertical wavenumber slopes from Argo is shown in Extended Data Fig. S5. These new estimates of ϵ are generally lower than the original ones, roughly by a factor 3-4, which also impairs the agreement with the reference data set [horizontal axis; 23]. Note, however, that this reference data set is also derived from Argo float observations, assuming a constant wavenumber slope s_M of 2. In a fully consistent comparison, we would have needed to account for the wavenumber slope bias also in this reference, which we do not attempt here owing to the high costs of creating such a global data set.

Regarding issue (iv), we follow [24] and investigate the sensitivity of the wavenumber slope estimates to the Turner angle [25]. The Turner angle Tu is defined as

$$Tu = atan\left(\alpha\frac{\partial\Theta}{\partial z} - \beta\frac{\partial S_A}{\partial_z}, \alpha\frac{\partial\Theta}{\partial z} + \beta\frac{\partial S_A}{\partial_z}\right), \tag{3}$$

where Θ is conservative temperature, S_A absolute salinity, α the thermal expansion coefficient and β the haline contraction coefficient. Double-diffusive convection is characterized by Turner angles between 45° and 90°, where positive angles represent the saltfinger and negative angles the diffusive regime. Both regimes describe an instability emerging in hydrostatically stable density profiles due to the vastly different molecular diffusivities of the tracers determining the density [i.e. heat and salt in the ocean, see e.g. 19].

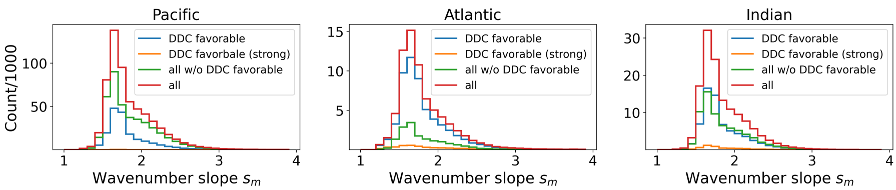

Fig. S6: Distribution of wavenumber spectral slope s_M in the Pacific, Atlantic and Indian Oceans, using (a) profiles with at least 50% of the Turner angle estimates meeting $45 < \|Tu\| < 90$ (DDC favorable); (b) profiles with at least 50% of the Turner angle estimates meeting $75 < \|Tu\| < 90$ (favorable to strong DDC); (c) all profiles except those identified in (a); (d) all profiles.

As illustrated in fig. S6, there is no clear change in the histograms when wavenumber slopes are estimated from profiles favorable to DDC compared to using all profiles or only those without a DDC imprint. We thus conclude that finescale contamination by DDC (issue iv) is not an important source of uncertainty for the wavenumber slope estimates, which represent averages over more than 2 million individual estimates.

Supplementary References

[1] Holloway, G.: Oceanic internal waves are not weak waves. Journal of Physical Oceanography **10**(6), 906–914 (1980)

[2] Müller, P., Holloway, G., Henyey, F., Pomphrey, N.: Nonlinear interactions among internal gravity waves. Reviews of Geophysics **24**(3), 493–536 (1986)

[3] McComas, C.: Equilibrium mechanisms within the oceanic internal wave field. Journal of Physical Oceanography **7**(6), 836–845 (1977)

[4] Nazarenko, S.: Wave Turbulence. Springer, Heidelberg (2011)

[5] Polzin, K.L., Lvov, Y.V.: Toward regional characterizations of the oceanic internal wavefield. Reviews of Geophysics **49 RG4003** (2011)

[6] Eden, C., Pollmann, F., Olbers, D.: Numerical evaluation of energy transfers in internal gravity wave spectra of the ocean. Journal of Physical Oceanography **49**(3), 737–749 (2019)

[7] Wu, Y., Pan, Y.: Energy cascade in the garrett-munk spectrum of internal gravity waves. arXiv preprint arXiv:2305.13110 (2023)

[8] Naveira Garabato, A.C., Meredith, M.: Ocean mixing: Oceanography at a watershed. In: Naveira Garabato, A.C., Meredith, M. (eds.) Ocean Mixing. Elsevier, Amsterdam (2022)

[9] Whalen, C.B., de Lavergne, C., Garabato, A.C.N., Klymak, J.M., Mackinnon, J.A., Sheen, K.L.: Internal wave-driven mixing: governing processes and consequences for climate. Nature Reviews Earth & Environment **1**(11), 606–621 (2020)

[10] Dematteis, G., Polzin, K., Lvov, Y.V.: On the origins of the oceanic ultraviolet catastrophe. Journal of Physical Oceanography **52**(4), 597–616 (2022)

[11] Ijichi, T., Hibiya, T.: Eikonal calculations for energy transfer in the deep-ocean internal wave field near mixing hotspots. Journal of Physical Oceanography **47**(1), 199–210 (2017)

[12] Polzin, K.L., Lvov, Y.V.: A one-dimensional model for investigating scale-separated approaches to the interaction of oceanic internal waves. arXiv preprint arXiv:2204.00069 (2022)

[13] Polzin, K.L., Garabato, A.C.N., Huussen, T.N., Sloyan, B.M., Waterman, S.: Finescale parameterizations of turbulent dissipation. Journal of Geophysical Research: Oceans **119**(2), 1383–1419 (2014)

[14] Polzin, K., Kunze, E., Toole, J., Schmitt, R.: The partition of finescale energy into internal waves and subinertial motions. Journal of physical oceanography **33**(1), 234–248 (2003)

[15] Kunze, E., Sanford, T.B.: Submesoscale dynamics near a seamount. part i: Measurements of ertel vorticity. Journal of physical oceanography **23**(12), 2567–2588 (1993)

[16] Joyce, T.M., Luyten, J.R., Kubryakov, A., Bahr, F.B., Pallant, J.S.: Meso- to large-scale structure of subducting water in the subtropical gyre of the eastern north atlantic ocean. Journal of physical oceanography **28**(1), 40–61 (1998)

[17] Thompson, A.F., Lazar, A., Buckingham, C., Garabato, A.C.N., Damerell, G.M., Heywood, K.J.: Open-ocean submesoscale motions: A full seasonal cycle of mixed layer instabilities from gliders. Journal of Physical Oceanography **46**(4), 1285–1307 (2016)

[18] Polzin, K., Ferrari, R.: Isopycnal dispersion in natre. Journal of physical oceanography **34**(1), 247–257 (2004)

[19] Stern, M.E.: The "salt-fountain" and thermohaline convection. Tellus **12**(2), 172–175 (1960)

[20] Schmitt, R.W.: Double diffusion in oceanography. Annual Review of Fluid Mechanics **26**(1), 255–285 (1994)

[21] Riley, J.J., Lelong, M.-P.: Fluid motions in the presence of strong stable stratification. Annual review of fluid mechanics **32**(1), 613–657 (2000)

[22] Kunze, E.: A unified model spectrum for anisotropic stratified and isotropic turbulence in the ocean and atmosphere. Journal of Physical Oceanography **49**(2), 385–407 (2019)

[23] Pollmann, F., Eden, C., Olbers, D.: Global finestructure estimates of internal wave energy levels and wave-induced mixing from Argo float profiles [Data set]. SEANOE. https://doi.org/10.17882/95327 (2023)

[24] Pollmann, F.: Global characterization of the ocean's internal wave spectrum. Journal of Physical Oceanography **50**(7), 1871–1891 (2020)

[25] Ruddick, B.: A practical indicator of the stability of the water column to double-diffusive activity. Deep Sea Research Part A. Oceanographic Research Papers **30**(10), 1105–1107 (1983)